Prediction of Slender Body Coning Characteristics

L. E. Ericsson*
Lockheed Missiles & Space Company, Inc., Sunnyvale, California 94088

At high angles of attack the asymmetric flow separation occurring on a slender forebody of revolution generates large asymmetric loads which can drive a missile or an aircraft in a coning motion. The limiting rate is obtained when the asymmetry-induced driving moment is balanced by the drag-induced damping moment. The paper describes how this limiting rate in the case of a pointed cone-cylinder can be predicted for laminar flow conditions using two-dimensional lift and drag data obtained in experiments with a rotating circular cylinder.

Nomenclature

D = cylinder diameter
d = local (cone) diameter
d^1 = sectional drag: coefficient $c_d = d^1/(\rho_\infty U_\infty^2/2)D$
l = body length
ℓ = cross-sectional lift: coefficient $c_\ell = \ell/(\rho_\infty U_\infty^2 2)D$
M = Mach number
N = coning rate
Re = Reynolds number, $= U_\infty D/\nu_\infty$
r = yawing rate
S = reference area, $= \pi D^2/4$
t = time
U_∞ = freestream horizontal velocity
U_W = wall velocity
V_L = lateral velocity
v_L = dimensionless lateral velocity, $= |V_L/U_\infty|$
x = distance from apex (Fig. 5)
Y = side force: coefficient $C_Y = Y/(\rho_\infty U_\infty^2/2)S$; $c_y = \partial C_Y/\partial(x/D)$
α = angle of attack
β = angle of sideslip
θ_c = cone semiangle
θ_N = semiangle of conic nose
ν = kinematic viscosity
ξ = dimensionless x coordinate, $= (x - x_{RC})/D$
ρ = fluid density
σ = total angle of attack, $= \arctan[(\tan^2\alpha + \tan^2\beta)^{1/2}]$
Ψ = coning angle
Ω = dimensionless coning rate, $= 2\pi ND/U_\infty$

Subscripts

A = apex
AS = asymmetric load
B = base
BC = start of base cone
D = drag
d = discontinuity
lam = laminar
NC = end of nose cone
RC = rotation center (Fig. 5)
turb = turbulent
W = wall
∞ = freestream conditions

Superscript

$\bar{}$ = time average

Differential Symbols

$\dot{\Psi}$ = $\partial\Psi/\partial t$; $\ddot{\Psi} = \partial^2\Psi/\partial t^2$
c_{ℓ_V} = $\partial c_\ell/\partial(U_W/U_\infty)$
C_{nr} = $\partial C_n/\partial(rl/2U_\infty)$
$C_{n_{\dot\beta}}$ = $\partial C_n/\partial(\dot\beta l/2U_\infty)$

Introduction

THE long slender nose of a missile or an advanced fighter aircraft, maneuvering at high angles of attack, experiences flow separation of various types. The flow separation generates not only large local aerodynamic forces but can also generate large downstream loads through the interaction by the shed vortices with downstream wing and tail surfaces. The separation-induced local side force can exceed the local normal force[1] and result in yawing moments far beyond the control capability of existing aircraft.[2]

Furthermore, interaction between the separation-induced vortices and downstream lifting surfaces can result in severe wing-rock oscillations, as has been demonstrated in wind-tunnel tests.[3] This wing-rock motion will be accompanied by a nose-slice motion, resulting from the coupling between the asymmetric nose load and the lateral motion of the nose. Such coupling in its purest form is exhibited by a slender body at high angles of attack, such as the observed coning motion of a cone-cylinder body[4] (Fig. 1). The coning started in one direction because of nose microasymmetries.[1] The authors state, however, that only a slight push in the opposite direction was needed to establish the mirror characteristics. That is, the so-called moving-wall effect[5] dominated over the static asymmetry. The purpose of the present paper is to describe analytic means by which the experimentally observed coning characteristics[4] can be predicted.

Analysis

Figure 1 shows the ranges of U_∞ and U_W/U_∞ covered in the test. It has been shown[1] that two-dimensional crossflow results can be applied to slender bodies at $\alpha > 30$ deg. The results for $\alpha = 90$ deg from the same test[4] (Fig. 2) show that critical flow conditions (for $U_W/U_\infty = 0$, i.e., $N = 0$) were established at $U_\infty > 25$ m/s. Thus, one can conclude that the results in Fig. 1 for $\alpha = 45$ deg were obtained with laminar flow conditions. Consequently, the laminar Magnus lift data[6] in Fig. 3 apply. The top insets in Fig. 3 illustrate how the (positive) Magnus lift is generated. As the moving-wall effect is concentrated to the flow region near the stagnation point, and, therefore, is very similar for rotating and translating circular cross sections,[7] it will generate a force that drives the coning motion.

The tested geometries[4] (Fig. 4) are represented in the analysis by the general geometry shown in Fig. 5. Based on experience, the separation asymmetry that produces asymmetric vortices is

Presented as Paper 89-2223 at the AIAA 7th Applied Aerodynamics Conference, Seattle, WA, July 31-Aug. 3, 1989; received Sept. 5, 1989; revision received Feb. 21, 1990.

*Senior Consulting Engineer. Fellow AIAA.

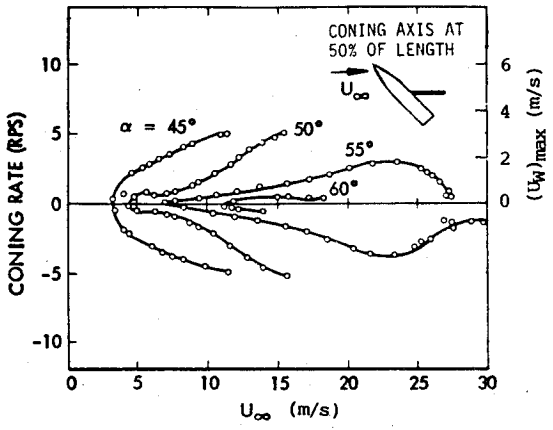

Fig. 1 Steady-state coning test of cone-cylinder body.[4]

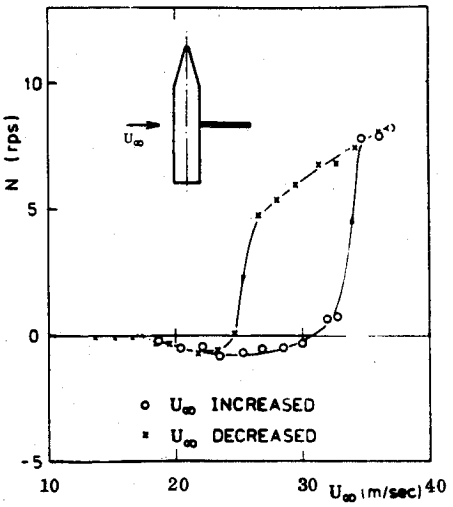

Fig. 2 Flat spin rate of cone-cylinder body.[4]

MODEL	θ_N	x_{cg}/l	DIMENSION (mm)
BLUNTED NOSE CONE-CYLINDER	15°	50 % 52.7 55.0 57.5 60.0 62.7	STANDARD 198.9 l = 275.0
	10°	56.1 60.5 64.9	313.2
	20°	46.5 51.9 60.1	257.1
SHARP NOSE CONE-CYLINDER	15°	57.7 (55.0)	292.2
TRUNCATED NOSE CONE-CYLINDER	15°	54.3 (55.0)	270.6
CYLINDER		50	250
BI-CONE CYLINDER	15°	50 (60)	350

( ) C.G. OF CORRESPONDING STANDARD MODEL

Fig. 4 Model geometrics for coning experiment.[4]

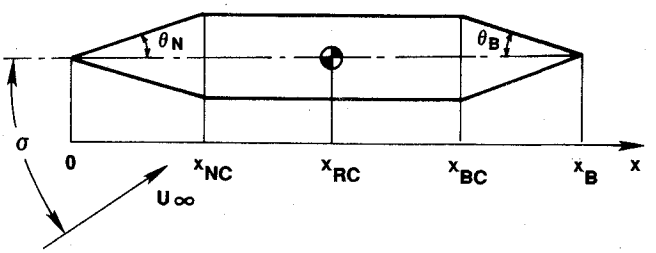

Fig. 5 Definition of geometric parameters.

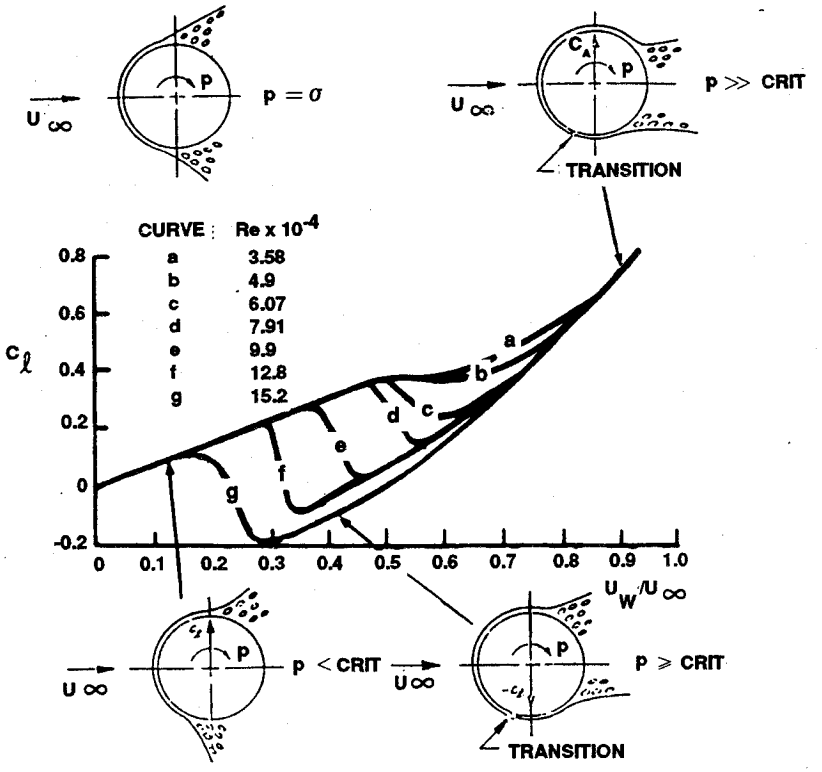

Fig. 3 Magnus lift of rotating circular cylinder for initially subcritical flow conditions.[6]

generated on the nose when it is slender.[1] Consequently, in the present case, it is assumed that the moving-wall effect is limited to the conical nose for the cone-cylinder geometries in Fig. 4. The bluff cylinder-alone geometry needs a different treatment, and it will be analyzed later. The driving coning moment, generated by the separation asymmetry on the conic nose, is balanced by the drag-generated damping moment from the full length of the body, resulting in a steady-state coning motion of a certain rate (Fig. 1). Although the flow visualization pictures, according to the authors, show a new asymmetric vortex pair developing aft of the rotation center, this "extra" vortex pair could have been started for reasons unrelated to the coning motion, as discussed in Ref. 1. Additionally, the moving-wall effects just behind the rotation center would be very small and are not likely to affect significantly the development of a new asymmetric vortex pair. The flow pictures show that the asymmetric vortex pair, generated by the nose, breaks away from the body at the nose-cylinder shoulder. This supports the assumption made here that the side force driving the coning motion is generated on the conic nose.

The magnitude of the coning-induced lateral velocity is (see Fig. 5)

$$|V_L| = \dot{\Psi}|x - x_{RC}| \sin\sigma \tag{1}$$

With $\Omega = \dot{\Psi}D/U_\infty$ and $\xi = |x - x_{RC}|/D$, Eq. (1) gives

$$v_L = \left|\frac{V_L}{U_\infty}\right| = \Omega\xi \sin\sigma \tag{2}$$

The asymmetric separation-induced side force is

$$\left(\frac{\partial C_Y}{\partial \xi}\right)_{AS} = \frac{d}{D} c_\ell \tag{3}$$

As only the moving-wall effect near the flow stagnation point is of importance, the side force c_ℓ can be obtained as follows:

$$c_\ell = c_{\ell_v} v_L \tag{4}$$

where $c_{\ell_v} = \partial c_\ell/\partial(U_W/U_\infty)$ is obtained from curve a in Fig. 3.

Based on the crossflow independence principle,[8] used successfully to determine crossflow lift on cylindrical aft bodies,[9,10] the drag-induced side force coefficient can be expressed as follows:

$$\left(\frac{\partial C_Y}{\partial \xi}\right)_D = \frac{d}{D} c_d v_L^2 \tag{5}$$

The drag force is, of course, generated along the full length of the body. Thus, one obtains the following equation for the steady-state coning motion ($x_A = 0$ in Fig. 5):

$$\int_{\xi_{NC}}^{\xi_A} \left(\frac{\partial C_Y}{\partial \xi}\right)_{AS} \xi d\xi = \int_0^{\xi_A} \left(\frac{\partial C_Y}{\partial \xi}\right)_D \xi d\xi + \int_0^{\xi_B} \left(\frac{\partial C_Y}{\partial \xi}\right)_D \xi d\xi \tag{6}$$

Combining Eqs. (2–6) gives

$$\Omega = \frac{c_{\ell_v}}{c_d \sin\sigma}\left[(1 + 2\xi_{NC}\tan\theta_N)\frac{\xi_A^3 - \xi_{NC}^3}{3} - \tan\theta_N \frac{\xi_A^4 - \xi_{NC}^4}{2}\right]$$

$$\left[\frac{\xi_{NC}^4}{4} + (1 + 2\xi_{NC}\tan\theta_N)\frac{\xi_A^4 - \xi_{NC}^4}{4} - 2\tan\theta_N \frac{\xi_A^5 - \xi_{NC}^5}{5}\right.$$

$$\left. + \frac{\xi_{BC}^4}{4} + (1 + 2\xi_{BC}\tan\theta_B)\frac{\xi_B^4 - \xi_{BC}^4}{4} - 2\tan\theta_B \frac{\xi_B^5 - \xi_{BC}^5}{5}\right]^{-1} \tag{7}$$

For the simple cone-cylinder geometry Eq. (7) simplifies to

$$\Omega = \frac{c_{\ell_v}}{c_d \sin\sigma}\left[(1 + 2\xi_{NC}\tan\theta_N)\frac{\xi_A^3 - \xi_{NC}^3}{3} - \tan\theta_N \frac{\xi_A^4 - \xi_{NC}^4}{2}\right]$$

$$\left[\frac{\xi_{NC}^4}{4} + (1 + 2\xi_{NC}\tan\theta_N)\frac{\xi_A^4 - \xi_{NC}^4}{4} - 2\tan\theta_N \frac{\xi_A^5 - \xi_{NC}^5}{5} + \frac{\xi_{BC}^4}{4}\right]^{-1} \tag{8}$$

For laminar flow conditions, $c_d \approx 1.2$ and, from Fig. 3, $c_{\ell_v} = \partial c_\ell/\partial(U_W/U_\infty) \approx 0.75$. The geometric definitions of the models tested are obtained from Fig. 4. Determining Ω from Eq. (8), or Eq. (7) for the biconic model, the $N = f(U_\infty)$ characteristics are defined as follows:

$$N(\text{HZ}) = \frac{\Omega}{2\pi D(m)} U_\infty(\text{m/s}) \tag{9}$$

Comparison of Prediction with Experiment

Figure 6 shows that the predicted coning characteristics at $\alpha = 45$ deg for the 15-deg cone cylinder with a sharp nose agree well with the experimental results.[4] The prediction neglects the effect of bearing friction on the test results (as it was not known). This accounts for the finite velocity U_∞ needed in the experiment before the aerodynamic moment was large enough to overcome the friction moment (so that the coning motion could start).

The experimental results demonstrate that during the spin-up portion ($U_\infty < 10$ m/s) the moving-wall effect dominates over the effect of nose microasymmetries. Rotating the nose to

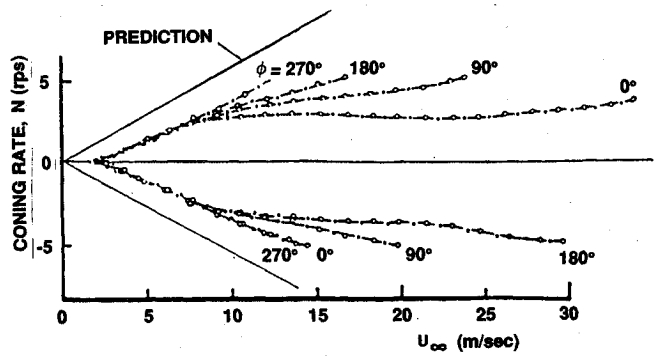

Fig. 6 Coning characteristics of the cone cylinder with a pointed nose.

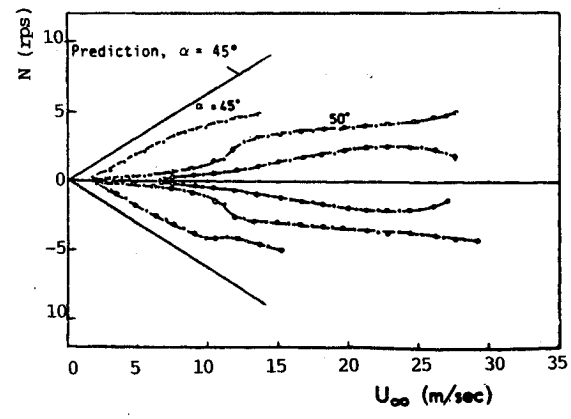

Fig. 7 Coning characteristics of the cone cylinder with truncated nose cone.

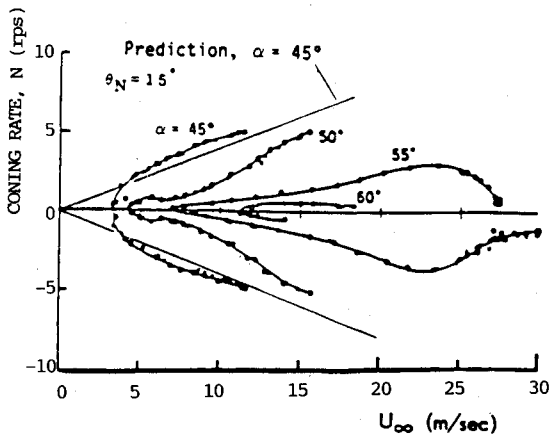

Fig. 8 Coning characteristics of the regular cone cylinder with hemispherical nose tip.

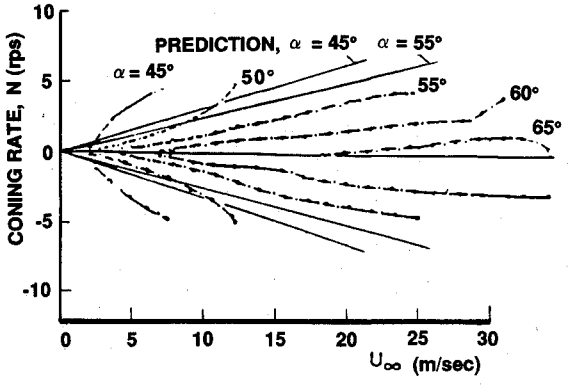

Fig. 9 Coning characteristics of cone cylinder with 20-deg conic nose.

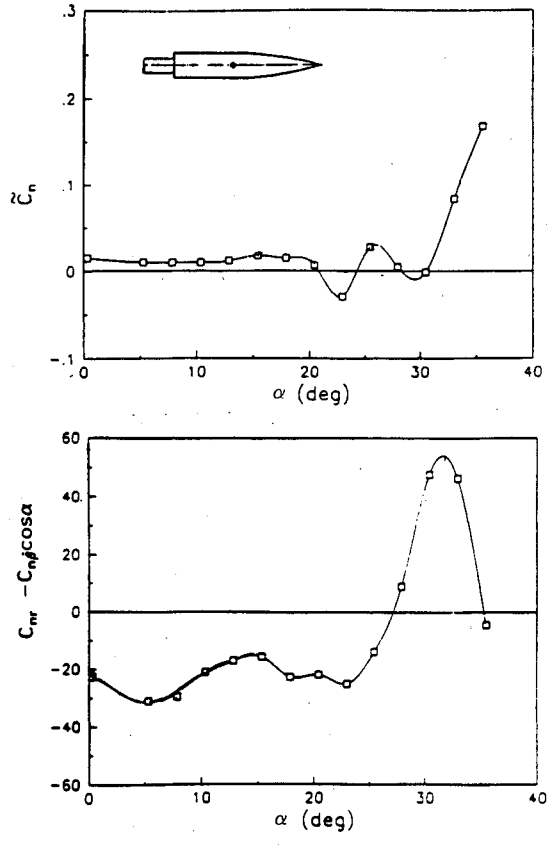

Fig. 10 Test results for ogive cylinder describing yawing oscillations at high angles of attack.[12]

different roll positions had no effect, contrary to the experience from static tests.[11] The sensitivity to the roll angle exhibited at $U_\infty > 10$ m/s is the likely result of beginning effects of critical flow conditions, where the effects of Reynolds number, freestream turbulence, and surface roughness compete with the moving-wall effect. One can visualize how the roll angle of the nose could determine the severity of the surface roughness that competes with the moving-wall effect at the local, incipient, critical flow condition.

Figure 7 shows that the coning characteristics at $\alpha = 45$ deg are also well predicted when 24% of the sharp nose tip is cut off (the truncated geometry in Fig. 4). However, when hemispherical roundness is added (the standard model in Fig. 4), the agreement deteriorates (Fig. 8). This is also true for the pointed cone cylinder when the cone angle is increased from 15 to 20 deg (Fig. 9). What can be the reason for this disagreement between prediction and experiment? For $\alpha = 45$ deg and $\theta_N = 20$ deg, $\alpha/\theta_N = 2.25$. Thus, on the $\theta_N = 20$ deg conic nose, incipient asymmetric flow conditions are realized for $\alpha = 45$ deg (Ref. 1). That means that it takes very little in the form of moving-wall effects to cause a complete "flip" of the separation asymmetry, explaining the vertical (90 deg) initial slope of the spin-up characteristics. A direct confirmation of this is provided by the experimental results obtained for an ogive cylinder describing yaw oscillations at moderately high angle of attack[12] (Fig. 10). As the apex half angle is $\theta_A = 16.3$ deg, incipient asymmetric flow conditions exist when α exceeds 32.6 deg. The figure shows that at this angle the undamping in yaw reaches its peak value.

Figure 10 also shows how the magnitude of the undamping decreases when the angle of attack is increased further. At the same time, the time-average value of the yawing moment starts to increase from the level close to zero existing when the yaw undamping peaks. That is, as the C_n bias increases (in Fig. 10 probably in some part due to tunnel wall interference[12]), which the moving-wall effect has to overcome, its potential to drive the oscillation is decreased. In the same manner, the bias due to nose microasymmetries will reduce the moving-wall effect for the $\theta_N = 20$ deg cone cylinder in Fig. 9. This would explain the experimental data trend, showing a decreasing rate of spin-up with increasing angle of attack. At $\alpha = 55$ deg, the value $\alpha/\theta_N = 2.75$ is reached, compared to $\alpha/\theta_N = 3$ in the case of the $\theta_N = 15$ deg cone cylinder at $\alpha = 45$ deg. In both cases, the α/θ_N value is well beyond the value for starting flow asymmetry, $\alpha/\theta_N \approx 2$, and the predicted spin-up shows good agreement with the measured initial spin-up (compare Fig. 6 for $\alpha = 45$ deg with Fig. 9 for $\alpha = 55$ deg).

The existence of an initial vertical spin-up slope also for the $\theta_N = 15$ deg cone cylinder at $\theta = 45$ deg (Fig. 8), when $\alpha/\theta_N = 3$, a value substantially larger than the incipient one, $\alpha/\theta_N = 2$, is the result of the nose bluntness, which delays the development of separation symmetry.[13] Thus, the conditions at $\alpha = 45$ deg may be at the end of the incipient asymmetric flow region, whereas they are at the start of this region for the pointed $\theta_N = 20$ deg cone cylinder at $\alpha = 45$ deg where $\alpha/\theta_N = 2.25$.

Oscillatory Coning

The reversal of the Magnus lift, caused by the moving-wall effect on boundary-layer transition[5,6] (Fig. 3), has its corollary in the observed[4] reversal of the coning motion of a blunt-faced cylinder at high angles of attack[1] (Fig. 11). Initially, flow asymmetry and/or minute surface irregularities set the separation asymmetry. The ensuing coning motion reinforces the effects of the asymmetry, as the laminar separation is delayed on the advancing side, generating positive coning velocity and spin acceleration ($\dot{\Psi}$ and $\ddot{\Psi} > 0$). However, the moving-wall effect eventually causes boundary-layer transition on the retreating side. This reverses the separation asymmetry and the coning motion starts to decelerate (i.e., $\dot{\Psi} > 0$ but $\ddot{\Psi} < 0$). Eventually, this results in accelerated coning in the opposite direction ($\dot{\Psi}$

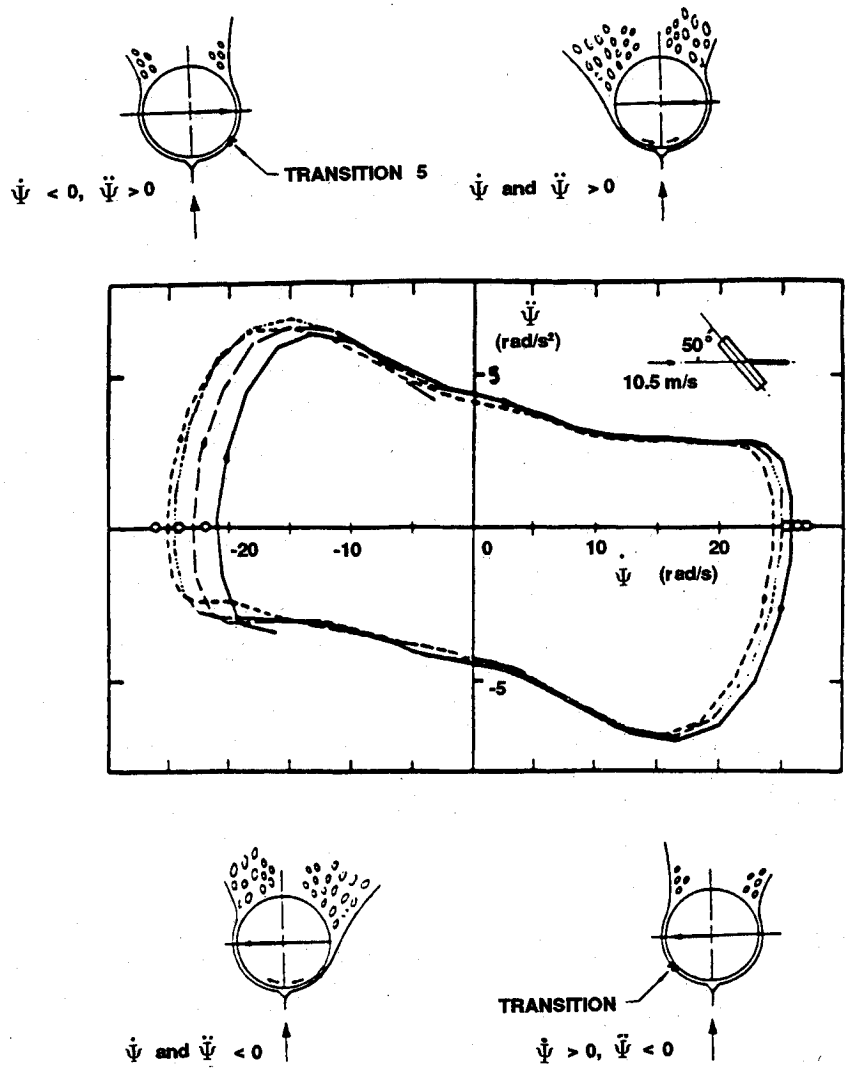

Fig. 11 Reversal of coning motion for a flat-faced circular cylinder.[1]

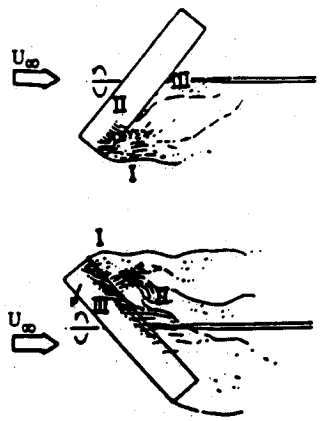

Fig. 12 Flow sketches from smoke flow visualization of coning flat-faced cylinder.[4]

and $\dot{\Psi} < 0$). The rotation reversal moves transition back into the wake on the new advancing side, and asymmetric laminar separation is re-established. Eventually, transition occurs on the retreating side to cause critical/subcritical separation, reversing the separation asymmetry and decelerating the coning motion ($\dot{\Psi} < 0$, $\ddot{\Psi} > 0$). The process continually repeats itself, resulting in a self-reversing, oscillatory coning motion.

The blunt-faced cylinder will have nose-induced separation already at $\alpha = 0$ (Ref. 14). As the flow visualization pictures reveal[4] (Fig. 12), the crossflow separation starts a distance aft of the nose, which measured in calibers is $\Delta\xi_A \approx 0.5 \tan\sigma$. Thus, for the standard cone cylinder, flying backward at $\alpha = 45$ deg, the asymmetric load distribution does not start until $\xi_A = 2.75 - 0.5 = 2.25$. In this case, the asymmetric load is assumed to be generated over the complete forebody ahead of the rotation center, that is $\xi_A = 2.25$ and $\xi_{NC} = 0$. With these values, Eq. (7) gives the prediction shown in Fig. 13. The agreement with the experimental results is good, except for the initial experimental data trend, which shows the same tendency toward an initial 90-deg spin-up slope as for the cone-forward position (Fig. 8). According to experiments,[15] the blunt-nose configuration should reach incipient asymmetric flow conditions at the nose when $\alpha = 4.2d/l = 43.5$ deg (see Ref. 1). Thus, incipient asymmetric flow conditions do exist at $\sigma = 45$ deg ($\alpha = 135$ deg in Fig. 13), explaining the experimental data trend.

Figure 14 shows the time histories at $U_\infty = 10.1$ m/s and $\alpha = 135$ deg of coning angle Ψ, coning rate $\dot{\Psi}$, and angular acceleration $\ddot{\Psi}$ (Ref. 4). It can be seen that the amplitude of the oscillatory coning is $\Delta\Psi = 110$ rad or 17.5 revolutions. The experimental results in Fig. 11 are in general agreement with the flow mechanisms postulated to cause the coning characteristics shown in Fig. 14. However, the acceleration data in Fig. 14 provide additional information about the moment driving the coning motion, showing it to be of larger magnitude during the deceleration phase of the motion. The time-average level seems to be 25–50% higher for deceleration than for acceleration.

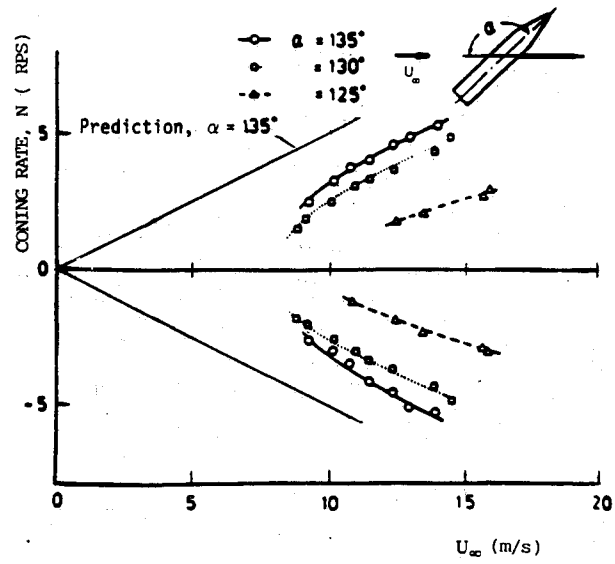

Fig. 13 Coning characteristics of regular cone cylinder flying backward.

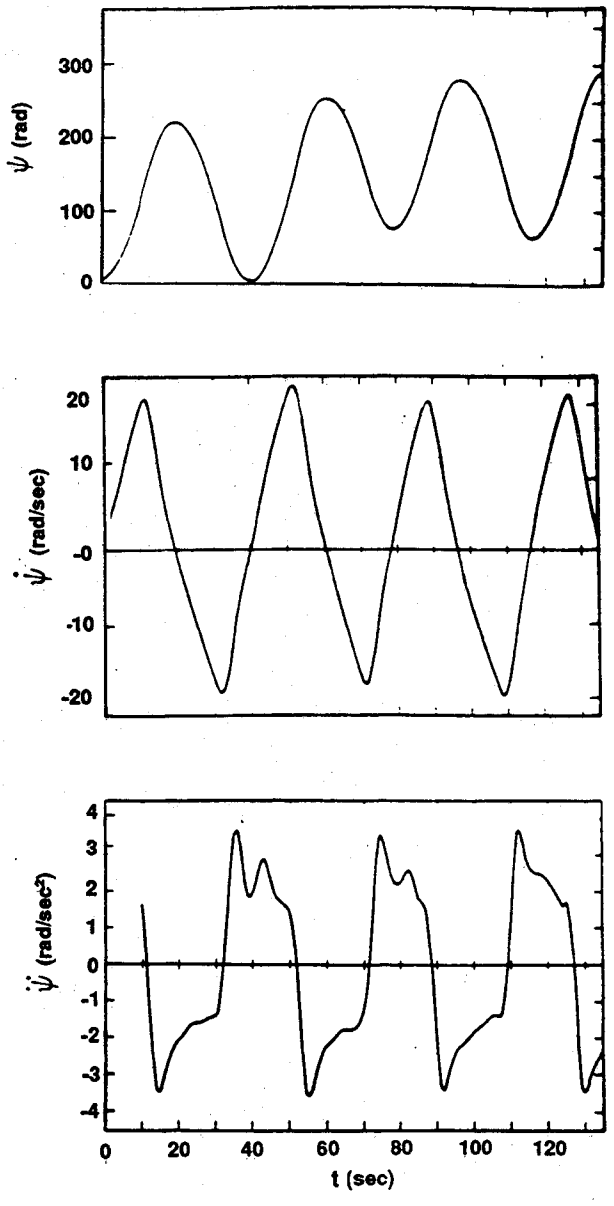

Fig. 14 Time history of coning angle ψ (t), angular rate $\dot{\Psi}$ (t), and angular acceleration $\ddot{\Psi}$ (t) of regular cone cylinder at $\alpha = 135$ deg.[4]

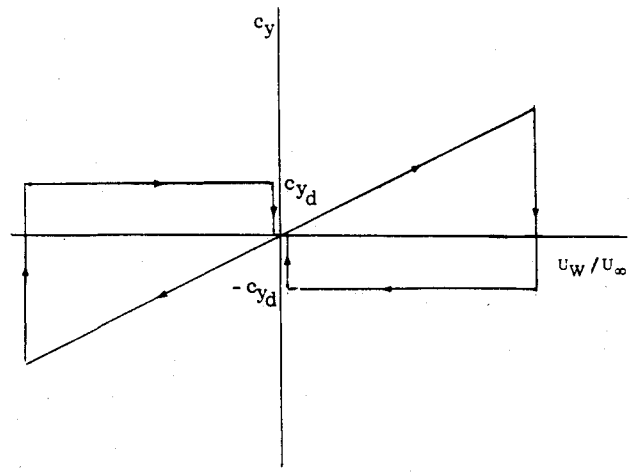

Fig. 15 Schematic side force characteristics for flat-faced cylinder.

From the discussion of Fig. 11 and the experimental results in Fig. 3, the picture sketched in Fig. 15 emerges for the variation of the local side force c_y with U_W/U_∞. Figures 1 and 2 show that the test data at $U_\infty = 10.1$ m/s in Fig. 14 were obtained for a Reynolds number that is 32–40% of the critical Reynolds number. That is, the Magnus lift data[6] for curve f in Fig. 3 would apply, giving $c_{yd} = c_{\ell d} \approx -0.1$ (see Fig. 15). Looking at Figs. 1 and 13, however, one finds that $U_W/U_\infty \leq 0.2$, which means that curve g in Fig. 3 rather than curve f would apply, giving $c_{yd} = c_{\ell d} \leq -0.2$.

In the case of the discontinuous side force reversal (Fig. 15), the driving side force $c_y = c_\ell$ is constant. Thus, Eq. (7) becomes (for $\theta_N = 90$ deg, $\xi_A = \xi_{NC} = 2.25$)

$$\Omega = \operatorname{cosec}\sigma\left(\frac{|c_\ell|}{c_d}\frac{\xi_A^2}{2}\right)^{1/2}\left[\frac{\xi_A^4}{4} + \frac{\xi_{BC}^4}{4} + (1 + 2\xi_{BC}\tan\theta_B)\frac{\xi_B^4 - \xi_{BC}^4}{4}\right.$$

$$\left. - 2\tan\theta_B\frac{\xi_B^5 - \xi_{BC}^5}{5}\right]^{-1/2} \qquad (10)$$

Reference 6 shows that for $U_W/U_\infty < 0.2$ the drag for curve g is $c_d \approx 1.1$, which, together with $|c_\ell| \approx 0.2$ in Eq. (10), gives $\Omega = 0.196$. With c_ℓ given by Eq. (4), one obtains $\Omega = 0.140$ for the acceleration phase. Thus, a 40% higher time-average level of the driving moment is predicted for the deceleration period. This compares favorably with the experimental data for $\ddot{\Psi}$ in Fig. 14.

Discussion

The developed method for prediction of slender-body coning characteristics has limited direct application by itself. This is true even in the case of laminar flow, as was exemplified by the incipient flow conditions illustrated in Figs. 8 and 9. Another limitation is that only one cell of asymmetric flow separation is allowed. It is shown in Ref. 16 how this leads to severe overprediction of the coning rate for very slender noses, such as a 10-deg conic nose, which has a sinusoidal type axial variation of the induced side loads.

In addition to these geometric limitations, the limitation to laminar flow prevents the application of the method to flow conditions that are not laminar, such as will usually be the case for the full-scale vehicle. For cases where turbulent flow dominates the aerodynamics, the present method could be applied directly by using the Magnus lift characteristics measured at supercritical initial flow conditions[6] (Fig. 16). This was done successfully in Ref. 16 to predict the measured coning characteristics of the 15-deg cone cylinder with sandpaper roughness on the conic nose.[4] However, in many cases the coupling between boundary-layer transition and vehicle motion has a

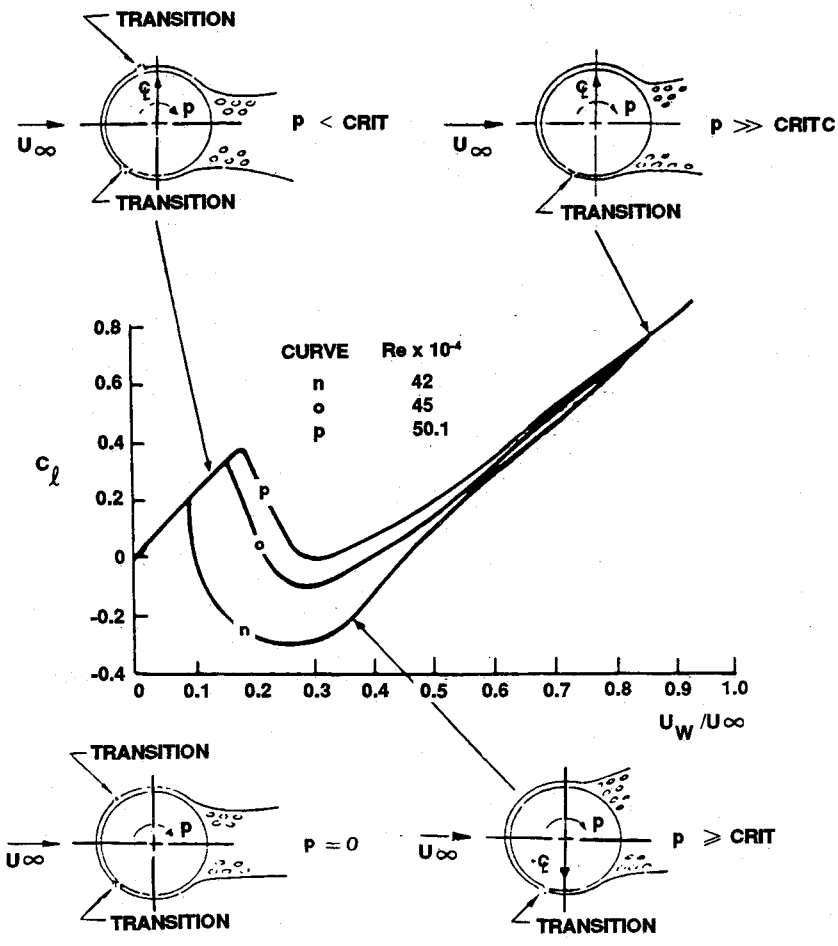

Fig. 16 Magnus lift of rotating circular cylinder for initially supercritical flow conditions.[6]

dominant effect on the high-alpha vehicle dynamics.[17] Consequently, methods will have to be developed for computation of the transition effect on high-alpha aerodynamics before prediction of full-scale coning and/or nose slice of missiles and aircraft will be possible.

Conclusions

Analytic means are described that can predict the coning motion characteristics of slender bodies, observed in subscale tests at laminar flow conditions. Extension of the analysis to higher Reynolds numbers should provide the means needed for prediction of the coning and nose-slice motions experienced by full-scale missiles and aircraft in free flight.

Acknowledgment

This paper is based on results developed under contract to Flight Dynamics Lab/FIGC, Wright Patterson AFB, Contract F33615-C-3607, monitored by W. B. Blake.

References

[1]Ericsson, L. E., and Reding, J. P., "Asymmetric Vortex Shedding from Bodies of Revolution," *Progress in Astronautics and Aeronautics: Tactical Missile Aerodynamics,* Vol. 104, edited by M. J. Hemsch and J. N. Nielsen, AIAA, New York, 1986, pp. 243–296, Chap. VII.

[2]McElroy, G. E., and Sharp, P. S., "An Approach to Stall/Spin Development and Test," AIAA Paper 71-772, July 1971.

[3]Brandon, J. M., and Nguyen, L. T., "Experimental Study of Effects of Forebody Geometry on High Angle of Attack Static and Dynamic Stability," AIAA Paper 86-0331, Jan. 1986.

[4]Yoshinaga, T., Tate, A., and Inoue, K., "Coning Motion of Slender Bodies at High Angles of Attack in Low Speed Flow," AIAA Paper 81-1899, Aug. 1981.

[5]Ericsson, L. E., "Moving Wall Effects in Unsteady Flow," *Journal of Aircraft*, Vol. 25, No. 11, 1988, pp. 977–990.

[6]Swanson, W. M., "The Magnus Effect: A Summary of Investigations to Date," *Journal of Basic Engineering*, Vol. 83, Sept. 1961, pp. 461–470.

[7]Ericsson, L. E., "Circular Cylinder Response to Karman Vortex Shedding," *Journal of Aircraft*, Vol. 25, No. 9, 1988, pp. 769–775.

[8]Schlichting, H., *Boundary Layer Theory*, translated by J. Kestin, McGraw-Hill, New York, 1955.

[9]Allen, J. H., "Estimation of the Forces and Moments on Inclined Bodies of Revolution of High Fineness Ratio," NACA RM A9126, 1949.

[10]Jorgensen, L. H., "Prediction of Aerodynamic Characteristics for Slender Bodies Alone and With Lifting Surfaces to High Angles of Attack," Paper 28, AGARD-CP-247, Oct. 1978.

[11]Keener, E. R., Chapman, G. T., Cohen, L., and Taleghani, J., "Side Forces on a Tangent-Ogive Forebody with a Fineness Ratio of 3.5 at High Angles of Attack and Mach Numbers from 0.1 to 0.7," NASA TMX-3437, Feb. 1977.

[12]Beyers, M., "Unsteady Wall Interference in Rotary Tests," AIAA Paper 89-0046, Jan. 1989.

[13]Ericsson, L. E., and Reding, J. P., "Alleviation of Vortex-Induced Asymmetric Loads," *Journal of Spacecraft and Rockets*, Vol. 17, No. 6, 1980, pp. 548–553.

[14]Ericsson, L. E., "Unsteady Aerodynamics of Separating and Reattaching Flow on Bodies of Revolution," *Recent Research on Unsteady Boundary Layers*, Vol. 1, IUTAM Symposium, Laval University, Quebec, May 1971, pp. 481–512.

[15]Fiechter, M., "Über Wirbelsysteme and schlanken Rotationskörpern und ihren Einfluss auf die aerodynamische Beiwerte," Bericht 10/66, Deutsch-Französisches Forchungs-Institut, Saint Louis, France, Dec. 1966.

[16]Ericsson, L. E., "Prediction of Slender Body Coning Characteristics," AIAA Paper 89-2223, Aug. 1989.

[17]Ericsson, L. E., "Effects of Transition on Wind Tunnel Simulation of Vehicle Dynamics," *Progress of Aerospace Sciences*, Vol. 27, 1990, pp. 121–144.

Clark H. Lewis
Associate Editor